Computers & Fluids 114 (2015) 218–231

Contents lists available at ScienceDirect

Computers & Fluids

journal homepage: www.elsevier.com/locate/compfluid

Numerical simulation of hydrodynamic wave loading by a compressible two-phase flow method

Rik Wemmenhove [a,1], Roel Luppes [a], Arthur E.P. Veldman [a,*], Tim Bunnik [b]

[a] Institute for Mathematics and Computer Science, University of Groningen, P.O. Box 407, 9700 AK Groningen, The Netherlands
[b] MARIN, P.O. Box 28, 6700 AA Wageningen, The Netherlands

ARTICLE INFO

Article history:
Received 3 January 2014
Received in revised form 3 January 2015
Accepted 11 March 2015
Available online 20 March 2015

Keywords:
CFD
Sloshing
Wave loading
Two-phase flow
VOF-method
Spurious velocities

ABSTRACT

Hydrodynamic wave loading on and in offshore structures is studied by carrying out numerical simulations. Particular attention is paid to complex hydrodynamic phenomena such as wave breaking and air entrapment. The applied CFD method, ComFLOW, solves the Navier–Stokes equations with an improved Volume-of-Fluid method to track the movement of the free surface. A local height function keeps the surface sharp (no 'flotsam and jetsam'). Application of two different fluid models, single-phase (only liquid) and two-phase (liquid and compressible gas) is presented, the latter model being capable of simulating bubbles of entrapped gas.

Treatment of the density around the free surface is found highly critical for obtaining an accurate fluid distribution and velocity field. A newly-developed gravity-consistent density averaging method is applied to prevent spurious velocities around the free surface. The convective terms are approximated by a compressible, symmetry-preserving second-order upwind discretization. Time integration, using second-order Adams–Bashforth, is carried out with a generalization of the familiar pressure-correction method, in which the full acoustical part of the flow equations is treated implicitly.

Numerical results are validated against experimental data for two test cases. As an example of internal wave loading, liquid sloshing dynamics are validated with experimental results for a 1:10 scale LNG tank section. In particular, the experimental pressure signal during a moment of air entrapment is compared with one-phase and two-phase flow simulations. The simulation of external wave loading is validated with data from an experiment with wave run-up against a 1:50 scale semi-submersible offshore structure. The test cases show that modeling of two-phase effects can be beneficial for simulating hydrodynamic wave loading.

1. Introduction

Offshore environments are known for their large variability in wind, waves and currents. Ships and offshore structures should be able to withstand environmental loads during violent weather conditions, even in case of steep, extreme, waves [13,18]. Awareness of the magnitude of these loads is important during design and operation [4]. In order to estimate wave loads on offshore structures by means of a numerical method, both the wave field and the structural geometry have to be modeled accurately and with sufficient detail. Linear methods, based on potential flow theory, to analyze the indicated extreme events are not capable of predicting wave loads to an acceptable level of accuracy. Especially near the objects studied, the physical phenomena accompanying these events are highly non-linear in relation to the occurring wave elevations, and require more complete models as a basis for describing wave dynamics and loads. The review paper [42] and the monograph [11] give well-balanced descriptions of the strengths and limitations of linear flow models.

Furthermore, in complex cases, modeling the dynamics of both water and the surrounding compressible air is helpful to estimate loads more accurately. The dynamics of the water and compressible air phases are well visible for complex free surface problems like green water loading, slamming and tank sloshing. In particular, around the free surface a complex interaction between water and air may occur. Spray, consisting of many small droplets, is observed above the free liquid surface, while clouds of small bubbles (entrained air) are present just below it. Wave overtopping, either due to wave steepness or the presence of an offshore structure, may lead to the entrapment of a much larger air pocket. Air pockets can have a cushioning effect on peak pressure levels during wave

* Corresponding author. Tel.: +31 503633939; fax: +31 503633800.
E-mail addresses: rwemmenhove@slb.com (R. Wemmenhove), r.luppes@rug.nl (R. Luppes), a.e.p.veldman@rug.nl (A.E.P. Veldman), t.bunnik@marin.nl (T. Bunnik).
[1] Present address: Schlumberger, P.O. Box 234, 1372 Asker, Norway.

http://dx.doi.org/10.1016/j.compfluid.2015.03.007
0045-7930/

impacts [33]. The size of these air pockets varies greatly, but they generally have a short lifetime [7]. The life cycle of air pockets is also influenced by aeration of the water, making the physics more complex with even smaller length scales and compressibility effects. This part of the physics lies outside the scope of the present paper: the water phase will be considered strictly incompressible. Also capillary effects from surface tension are not considered, but can be added if desired [30].

The entrapment of air pockets and the entrainment of bubbles is not only important for wave loading on ships and offshore structures (external wave loading), but also for internal wave loading cases, such as the fluid motion in fuel tanks or anti-roll tanks on board of a ship. Model test campaigns to predict the air–water interaction during hydrodynamic wave loading are rather costly and time-consuming. Therefore, there is a great need for numerical simulation tools that can predict the impact loading on and the flow around offshore structures during hydrodynamic wave loading.

To model two-phase flow effects for wave-type problems, a number of choices have to be made with respect to the numerical method. The description of the fluid flow of both phases is based on the Navier–Stokes equations. These equations can be applied to both phases separately, but in the current method the liquid and gas phase are described as one aggregated fluid with varying properties. Another important aspect is the choice of the computational grid. The grid should be constructed such that the free surface is described as 'sharp' as possible in order to model its dynamical behavior sufficiently accurate.

Instead of using a Cartesian grid, as in the present method, another option would be to construct an unstructured grid using a Lagrangian approach. However, aligning the grid with a moving interface results in a less transparent grid and is very difficult for highly distorted and rapidly moving free surfaces, as is the case in many offshore problems. An alternative for grid-based methods could be the use of Smoothed Particle Hydrodynamics (SPH) and related methods, e.g. [12,16,24,31]. These meshless methods put a large number of particles in the flow, each with their own mass and velocity [21]. They are however computationally expensive and lead to a less accurate pressure prediction, which is a major drawback when forces on offshore structures have to be computed.

In the method described in this paper, the Navier–Stokes equations are solved for compressible two-phase flow with an incompressible liquid phase and a compressible air phase. This occurs in such a way that the free surface is kept sharp even for violent flow conditions. The description of the interface is based on the Volume of Fluid (VOF) method, which has been introduced by Hirt and Nichols [19], extended with a local height function for improved accuracy [26,43]. The improved Volume of Fluid (iVOF) method is able to keep the interface sharp, while it allows use of a rather coarse grid to limit computation times.

Especially on staggered computational grids, two-phase flow models can suffer from serious errors near the free surface in the form of so-called spurious (or parasitic) velocities, see e.g. [14,17,38,39]. The cure is often sought in a more accurate treatment of reconstruction and/or advection of the free surface. In the present paper, however, we focus on the discrete compatibility between the pressure gradient, the density and the gravity force. A 'gravity-consistent' averaging of the density between cell centers and cell faces is found to play an essential role.

Generalizing the pressure Poisson equation for incompressible flow, in our compressible flow model the acoustical part is treated in an implicit way. The continuity equation (with the density implicitly coupled to the pressure) and the momentum equation are combined into a hyperbolic wave-type equation from which the pressure can be calculated. The convective terms are discretized with a compressible symmetry-preserving upwind method [20,44,49].

The numerical method, called ComFLOW, has been developed initially to simulate one-phase flow. Earlier applications were in the simulation of sloshing on board spacecraft [15,43,47], in medical science [28,29] and in μ-gravity biology [32]. Currently, the method is used to solve engineering problems in the maritime and offshore industry, e.g. [3,6,22,23,25–27]. Extensive validation with model experiments that are relevant for the offshore industry is an important aspect in the development of the numerical method. An overview of the current status of ComFLOW can be found in e.g. [45,46] and from the ComFLOW website [5] (containing also some experimental data).

The basics of the numerical method are presented first, after which attention is paid to the numerical refinements around the free surface. The method is validated with the results of two series of model experiments. The sloshing fluid motion inside a partially-filled LNG (liquefied natural gas) tank has been measured to validate the fluid flow inside closed domains. To test the simulation of impact phenomena and wave propagation, experiments concerning wave run-up against a semi-submersible offshore structure have been carried out. For the latter flow case an extensive assessment of numerical and experimental uncertainty is included.

2. Mathematical model

2.1. Aggregated governing equations

The flow of two phases is described as the flow of one aggregated fluid with varying properties, which can be described by one continuity and one momentum equation. This approach leads to a smooth velocity field around the free liquid surface [41]. Mass conservation is applied on an arbitrary part Ω of the flow domain with boundary S and an outward directed normal vector $\mathbf{n}$:

$$\int_\Omega \frac{\partial \rho}{\partial t}\,\mathrm{d}\Omega + \oint_S (\rho \mathbf{u})\cdot \mathbf{n}\,\mathrm{d}S = 0, \tag{1}$$

with $\mathbf{u} = (u, v, w)^T$ the velocity, ρ the density and t the time. Momentum conservation is given by

$$\int_\Omega \frac{\partial(\rho\mathbf{u})}{\partial t}\,\mathrm{d}\Omega + \oint_S (\rho\mathbf{u}\cdot\mathbf{n})\mathbf{u}\,\mathrm{d}S + \oint_S p\mathbf{n}\,\mathrm{d}S - \oint_S \{\mu(\nabla\mathbf{u} + \nabla\mathbf{u}^T) - \frac{2}{3}\mu(\nabla\cdot\mathbf{u})\mathbf{I}\}\cdot\mathbf{n}\,\mathrm{d}S - \int_\Omega \rho\mathbf{F}\,\mathrm{d}\Omega = 0, \tag{2}$$

with pressure p, dynamic viscosity μ and external force $\mathbf{F}$. For later use, we will reformulate these equations in other formats:

$$\frac{\partial\rho}{\partial t} + \nabla\cdot(\rho\mathbf{u}) = 0 \iff \frac{D\rho}{Dt} + \rho(\nabla\cdot\mathbf{u}) = 0 \ \text{ and } \ \frac{\partial\mathbf{u}}{\partial t} + \frac{1}{\rho}\nabla p = \mathbf{R}, \tag{3}$$

where $\mathbf{R}$ contains the convective and diffusive terms as well as the body force. The form of the momentum equation in (3) has been chosen because the quotient $\rho^{-1}\nabla p$ is constant for a hydrostatic pressure in two-phase flow, although ρ as well as ∇p are discontinuous between the two phases. That means that one can 'safely' calculate discrete derivatives of this expression, as will be needed in the sequel.

Given the variable density ρ in the mass and momentum equations, an additional equation of state $\rho = \rho(p)$ has to be applied to describe the compressibility of the air phase. Currently, the polytropic equation of state is used, i.e.

$$\frac{\rho}{\rho_{ref}} = \left(\frac{p}{p_{ref}}\right)^{1/\gamma} \quad \text{with} \quad \gamma = 1.4. \tag{4}$$

In this equation, the initial (atmospheric) reference values for pressure and density are used [51].

2.2. Boundary conditions

The no-slip boundary condition ($\mathbf{u} = 0$) is used at solid walls and objects within the computational domain. Inflow and outflow boundary conditions are specified in case of open boundaries.

Incoming waves at the inflow boundary are specified by prescribing the incoming velocity. The incoming wave is usually prescribed as a linear wave or a regular 5th order Stokes wave [40], but can also be described as a superposition of cosines, each with their own amplitude, frequency, wave number and phase (design wave).

The outflow boundary requires special attention, as some of the wave components may not propagate through but reflect against the boundary. Conventional boundary conditions, such as the Von Neumann and Sommerfeld outflow boundary conditions, are available in the numerical method. The disturbing effect of wave reflections on the fluid distribution can be reduced by putting the boundaries further away from the flow region of interest, but there are 'smarter' methods that reduce the necessary amount of grid cells. One method that reduces the effect of reflections is the use of a numerical beach [25], however, this requires extension of the flow domain by at least one wavelength downstream of a structure.

To keep the computational domain as small as possible while minimizing reflections at boundaries, a Generating and Absorbing Boundary Condition (GABC) has been developed recently [9,46,50]. This boundary condition, at inflow as well as outflow boundaries, implicitly computes at each location a 'local' average phase velocity c for the outgoing wave at the boundary, and combines it with the corresponding Sommerfeld condition. The reduction of reflections against the (artificial) numerical boundaries improves the description of the wave field and makes it possible to locate the in- and outflow boundaries close to the interesting flow area around a structure. The computational domain can be made much (two times or more) smaller than when a numerical beach is used, which reduces the computational costs considerably. We hope to report in more detail about this novel approach in forthcoming publications, e.g. [10].

2.3. Equation for the pressure

In case of incompressible flow, the continuity equation and the momentum equation can be combined into a Poisson equation for the pressure. The latter is solved implicitly, thus dealing with the infinite propagation speed of pressure waves in incompressible flow. For the compressible flow in the air phase this propagation speed is finite, but still large; therefore we generalize the incompressible approach. Combining the second form of the continuity equation and the momentum equation in (3) leads to

$$\nabla\left(\frac{1}{\rho}\cdot\nabla p\right) - \frac{\partial}{\partial t}\left(\frac{1}{\rho}\frac{D\rho}{Dt}\right) = \nabla\cdot\mathbf{R} \quad \Longleftrightarrow$$
$$\nabla\left(\frac{1}{\rho}\cdot\nabla p\right) - \frac{\partial}{\partial t}\left(\frac{1}{\rho c^2}\frac{Dp}{Dt}\right) = \nabla\cdot\mathbf{R} \tag{5}$$

(recall $\mathrm{d}p/\mathrm{d}\rho = c^2$). We recognize this to be a generalized hyperbolic wave equation for the pressure, which preferably is treated implicitly like its incompressible limit ($c \to \infty$) as used in the liquid phase. In the numerical approach we will not discretize this equation directly, but instead combine the discrete versions of the continuity equation and the momentum equation in (3). Yet, the result will be recognizable as a discretization of (5).

3. Numerical discretization

The computational domain is covered by a fixed Cartesian grid. The variables are staggered, with velocities defined on cell faces, whereas pressure and density are defined in cell centers. As described extensively in [25], the presence of solid body geometries is indicated by volume apertures and edge apertures. After identifying which grid cells are open for fluid flow, the 'open' cells are labelled as E(mpty), S(urface) and F(luid) cells. The discretization makes use of so-called cut-cells and takes account of the symmetries of the underlying equations [8].

For two-phase flow calculations, the flow characteristics are resolved in all open cells. This is considered advantageous, as it prevents from mass conservation problems (leading to local pressure spikes) that have been observed in one-phase simulations with rapid free surface advection [52]. During every computational time step, the pressure value is calculated first, after which density, velocity field and the position of the free surface are updated. In the following sections we will address the numerical issues near the free surface in more detail; but see also [51].

3.1. Momentum equation

The convective terms are discretized such that they do not interfere with the evolution of kinetic energy (unless diffusion is explicitly added, as in an upwind method). Relevant in this respect is

$$\begin{aligned}\frac{\partial}{\partial t}(\rho E_k) \equiv \frac{\partial}{\partial t}\left(\frac{1}{2}\rho\mathbf{u}\cdot\mathbf{u}\right) &= (\rho\mathbf{u})\cdot\frac{\partial\mathbf{u}}{\partial t} + \frac{1}{2}(\mathbf{u}\cdot\mathbf{u})\frac{\partial\rho}{\partial t}\\ &= -(\rho\mathbf{u})\cdot(\mathbf{u}\cdot\nabla\mathbf{u} + \text{pressure \& diffusion})\\ &\quad -\frac{1}{2}\mathbf{u}\cdot\mathbf{u}\nabla\cdot(\rho\mathbf{u}) = -\mathbf{u}\cdot\left\{(\rho\mathbf{u})\cdot\nabla + \frac{1}{2}\nabla\cdot(\rho\mathbf{u})\right\}\mathbf{u}\\ &\quad + \text{pressure \& diffusion}.\end{aligned} \tag{6}$$

In particular, the discrete version of the operator between the curly braces in (6) is designed to be skew-symmetric, such that the convective terms keep the energy unaffected [20,37,49].

For ease of presentation, we will discuss the discrete time integration by means of a forward-Euler method, although most of the simulations have been carried out with a (more accurate) Adams–Bashforth method. The latter method is in particular attractive in combination with a second-order upwind scheme for the convective terms in $\mathbf{R}$. Compared with its first-order variant [44], the second-order upwind scheme leads to a smaller artificial viscosity, especially in the second (air) phase, making it a better choice in terms of kinetic energy dissipation [51].

Thus, for forward Euler, the time-discrete version of (3) reads

$$\frac{\rho^{(n+1)} - \rho^{(n)}}{\delta t} + \mathbf{u}^{(n)}\cdot\nabla\rho^{(n)} + \rho^{(n)}\nabla\cdot\mathbf{u}^{(n+1)} = 0, \tag{7}$$

$$\frac{\mathbf{u}^{(n+1)} - \mathbf{u}^{(n)}}{\delta t} + \frac{1}{\rho^{(n)}}\nabla p^{(n+1)} = \mathbf{R}^{(n)}, \tag{8}$$

where the old and new time level are denoted by $\cdot^{(n)}$ and $\cdot^{(n+1)}$, respectively.

3.2. Pressure calculation

By eliminating $\mathbf{u}^{(n+1)}$ from (7) and (8), an equation for the pressure is obtained:

$$\nabla\cdot\left(\frac{1}{\rho^{(n)}}\nabla p^{(n+1)}\right) = \frac{1}{\rho^{(n)}\delta t}\left\{\frac{\rho^{(n+1)} - \rho^{(n)}}{\delta t} + \mathbf{u}^{(n)}\cdot\nabla\rho^{(n)}\right\} + \nabla\cdot\left(\frac{\mathbf{u}^{(n)}}{\delta t} + \mathbf{R}^{(n)}\right). \tag{9}$$

We recognize a generalization of the 'incompressible' Poisson equation for the pressure. Note that the first term in the right-hand side of (9) corresponds with the second-order time derivative in (5); this term has to be treated implicitly (cf. the superscript $\cdot^{(n+1)}$).

The term between curly braces in the right hand side stems from the continuity equation. As the density may vary up to a

factor of 1000 in space or time around the free surface, the two embraced terms separately can become large. Note, however, that their combination represents the discrete Lagrangian derivative $D\rho/Dt$. Analytically, when a point changes between air and liquid the two constituents of this term, $\partial\rho/\partial t$ and $\mathbf{u}\cdot\nabla\rho$, become δ-functions in time and space, respectively. Apart from compressibility effects, these constituents cancel analytically, but discretely this requires some careful maneuvering.

Hereto, denote the open fraction of a cell by F_b and the liquid fraction in a cell by F_s, then the gas fraction is $F_b - F_s$. With this notation, the discrete cell-averaged density ρ is defined by

$$\rho = \frac{F_s}{F_b}\rho_l + \frac{F_b - F_s}{F_b}\rho_g. \tag{10}$$

Noting that $DF_s/Dt = 0$, in the Lagrangian derivative we only have to take account of the gas density ρ_g. Thus the expression between braces in (9) can be reduced to the discrete version of

$$\frac{D\rho}{Dt} = \frac{F_b - F_s}{F_b}\frac{D\rho_g}{Dt} = \frac{F_b - F_s}{F_b}\left(\frac{\partial\rho_g}{\partial t} + \mathbf{u}\cdot\nabla\rho_g\right). \tag{11}$$

As the gas density ρ_g is relatively small and reasonably continuous in space and time, in contrast to the cell-averaged density ρ which reacts strongly on changes in F_s, this expression never contains large contributions which have to cancel.

Finally, the equation of state (4) is used to express the gas density in (11) in terms of the pressure at the new time level: $\rho_g^{n+1} = \rho_g(p^{n+1})$. Thus, before transferring this highly-nonlinear term to the left-hand side of the Poisson-like equation, it is linearized by a Newton approximation to eliminate the exponent $1/\gamma$ in the equation of state (4). After that, the system matrix of (9) is solved by a Krylov-subspace solver; details can be found in [51]. This class of solvers, with some form of preconditioning (in our case ILU), is well suited for Poisson-like equations with inhomogeneous coefficients (as is the case for large variations in the density), because they efficiently spread information across the computational domain. A disadvantage is their non-trivial parallelization. Therefore, in one-phase flow simulations the pressure is solved using a, highly parallelizable, SOR (Successive Over Relaxation) method, where the optimal relaxation parameter is determined during the iteration process [2]. Especially in the early days of vector computing, when the ComFLOW development started, this method ran at about 75% of a computer's maximum speed [48], which outweighed its relatively slow convergence. On modern parallel computer architectures, this advantage again becomes relevant.

4. Towards a sharp free surface

The free surface has to be kept sharp within one grid cell to be able to resolve violent flow conditions with breaking waves, droplets and bubbles accurately. Given the large density ratio around the interface, particular attention has to be paid to the density definition in cell centers and at cell faces.

4.1. Free surface description

As the free surface position is changing in time, the liquid filling ratios F_s and the free surface labels have to be recomputed every computational time step. In principle, the free surface is described by the equation $F_s(\mathbf{x}, t) = 0$, with the motion described by

$$\frac{DF_s}{Dt} = \frac{\partial F_s}{\partial t} + \mathbf{u}\cdot\nabla F_s = 0 \tag{12}$$

The displacement of the free surface is done in two steps. First the free surface is reconstructed and after that it is advected to the new position. The original VOF reconstruction method [19] uses Simple Linear Interface Calculation (SLIC), where the interface only consists of line segments that are parallel or perpendicular to the major flow axes. With this approach there exist discontinuities of the free surface. When using the piecewise linear reconstruction method (PLIC), introduced by Youngs [56], there are still free surface discontinuities at the cell edges and there is a jump in the free surface angle at each cell edge [15]. In three dimensions, the PLIC method represents the interface by oblique planes, and especially then the reconstruction of the free surface by the PLIC method would lead to strongly enhanced computational costs.

4.2. Local height function

A characteristic drawback of the SLIC method is the unphysical creation of flotsam ('floating wreckage') and jetsam ('jettisoned goods'). These phenomena concern isolated, submesh-size droplets disconnected from the free surface because of errors induced by the free surface reconstruction [36]. To prevent from flotsam and jetsam, a local height function has been introduced in the numerical method [15]. For the original VOF method without height function, the VOF-values are rounded off at the end of the displacement algorithm (values below zero are reset to zero and values above one are reset to one), leading to significant gains or losses in liquid mass, up to several percents of the initial water mass [25].

To determine the local height function, first the orientation of the free surface is determined (horizontal or vertical) depending on the values of the liquid filling ratio F_s in the surrounding block of cells. After that, the horizontal or vertical local height in each row or column in this block is determined by summing the VOF fractions (see Fig. 1). The local height function is applied in a 3×3 block (in 2D) or a $3 \times 3 \times 3$ block (in 3D) of cells surrounding a surface cell. Although other numerical methods take more grid cells (e.g. 3×5 or 3×7 in [1]) into account to determine the height function, using a $3 \times 3(\times 3)$ block is sufficient in the current numerical method. This is because the free surface is always captured in one grid cell (the central grid cell in Fig. 1). In Fig. 1, the orientation of the free surface is horizontal. When the free surface would cut the upper and lower edge of the central grid cell in Fig. 1, the height function is constructed from a vertical instead of a horizontal orientation of the free surface. By using the local height function, flotsam and jetsam are no longer present. Also, the loss of water is much smaller than with the original VOF method [25].

4.3. Gravity-consistent discretization

Discretization of the density is not only important for the unsteady term in the continuity Eq. (1), but also for several terms in the momentum Eq. (2). Given the staggered arrangement of grid variables, pressure and density are both defined and computed in cell centers. For compressible two-phase flow, the discrete density in the cell center is calculated as in (10), showing that the density is a function of the liquid cell fractions F_s and F_b and, by the equation of state, the pressure p. Although the density is coupled to the pressure value in the cell centers, the staggered variable arrangement requires computation of densities at cell edges as well.

An obvious way of defining cell-edge values for the density seems to be to average the adjacent cell-center values. As the latter are themselves averages of the density over the cell, we call this a cell-weighted averaging. However, the literature learns that it is not that straightforward. Spurious velocities have been observed in several numerical methods, e.g. [14,17,38,39]. It is argued that these anomalies could be reduced by improving the estimate of the free surface curvature [38], by improving the flow algorithms [39], or by improving the surface tension description [14]. Francois et al. [14] addresses spurious velocities to the numerical imbalance of the surface tension and the associated pressure

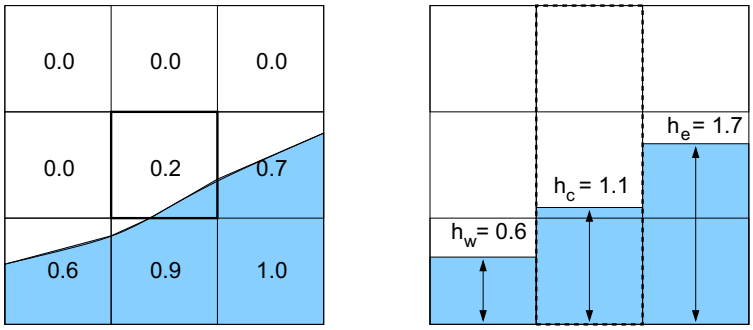

Fig. 1. Construction of the local height function in a 3×3 block for a central S-cell.

gradient. Their method reduces the spurious velocities for zero-gravity surface tension dominated cases. For offshore applications, however, the pressure gradient should also be in balance with the gravity force as the gravity forcing is usually much larger than the surface tension force.

The origin of the spurious velocities can be understood from a mismatch between the pressure gradient and the volume body force $\rho\mathbf{F}$. Let us consider an equilibrium condition with gravity, i.e. analytically $\nabla p = \rho\mathbf{g}$ holds. This equality should also hold in the discrete setting: $\rho\mathbf{g}$ should be a discrete gradient, i.e. we should have a discrete version of $\nabla \times (\rho\mathbf{g}) = 0$. This condition then defines the way in which the discrete density has to be averaged, as will be shown next.

To study the hydrostatic pressure and the related density averaging, we choose a coordinate system that is not aligned with the gravity vector. In this system, we consider a stratified equilibrium situation, where $\rho = f(z - \alpha x)$ with a gravity vector perpendicular to the isolines, i.e. $g_x = -\alpha g_z$. Then, analytically it easily follows that $\nabla \times (\rho\mathbf{g}) = 0$. For each contour integral, in particular the contour *ABCDA* in Fig. 2, one analytically has

$$0 = \oint \rho\mathbf{g} \cdot \mathrm{d}\mathbf{S} \equiv \int_A^B \rho g_x \,\mathrm{d}x + \int_B^C \rho g_z \,\mathrm{d}z + \int_C^D \rho g_x \,\mathrm{d}x + \int_D^A \rho g_z \,\mathrm{d}z.$$

Observe that the sides *BC* and *DA* together end up with a net contribution of $g_z(\rho_l - \rho_g)\alpha\delta x$, which cancels exactly against the contribution of the horizontal sides $g_x(\rho_l - \rho_g)\delta x$. We want to mimic this property as good as possible in the discretization, when we approximate each individual integral using the density value in the midpoint. For instance, for the side *BC* we would require

$$\rho_b \,\delta z := \int_B^C \rho \,\mathrm{d}z = \rho_l e_1 + \rho_g e_2. \tag{13}$$

This then defines the density average ρ_b in the face midpoint such that the influence from the gravitational body force (i.e. the hydrostatic pressure) is treated exactly. Therefore we call this a *gravity-consistent* averaging. It corresponds with an averaging over the momentum control volume around the face under consideration, i.e. the two *half* cells adjacent to the face. In contrast, the cell-weighted averaging discussed in the beginning of this section uses the two *full* cells adjacent to the face. Although explained in 2D, note that the phrasing of the last paragraph also applies to 3D.

Another way of deriving (13) is to demand that $p_C - p_B = \int_B^C \frac{\partial p}{\partial z}\,\mathrm{d}z$ also holds discretely. However, the derivative of p is not constant along this interval, but the combination $\frac{1}{\rho}\frac{\partial p}{\partial z}$ is. This suggests to write (compare [55, p. 86])

$$p_C - p_B = \int_B^C \frac{\partial p}{\partial z}\,\mathrm{d}z = \int_B^C \left(\frac{1}{\rho}\frac{\partial p}{\partial z}\right)\rho \,\mathrm{d}z \approx \left(\frac{1}{\rho}\frac{\partial p}{\partial z}\right)_b \int_B^C \rho \,\mathrm{d}z \approx \frac{1}{\rho_b}\frac{p_C - p_B}{\delta z}(\rho_l e_1 + \rho_g e_2).$$

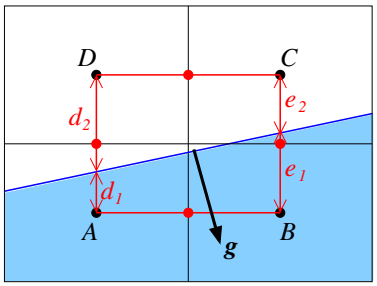

Fig. 2. Contour near free surface to explain gravity-consistent density averaging.

The third step makes use of the smoothness of $\frac{1}{\rho}\frac{\partial p}{\partial z}$, whereas the final step defines the density value ρ_b. This again leads to the density averaging (13).

Fig. 3 shows velocity vectors from two calculations for an equilibrium surface as discussed in Fig. 2. The cell-weighted averaging (Fig. 3(a)) clearly shows spurious velocities, whereas they disappear when gravity-consistent averaging is used (Fig. 3(b)).

Not only for the case in Fig. 3, but also for more realistic test cases, such as the sloshing motion of fluid inside a tank (which is described in more detail in Section 5), the spurious velocities disappear and the description of the free surface improves. This is illustrated in Fig. 4. The cell-weighted density averaging method leads to an unphysically irregular free surface, with many small droplets in the air above the free surface, see Fig. 4(a). Furthermore, flow velocities in the enclosed air above the free surface are relatively high compared with the flow velocities in the liquid phase. When applying the gravity-consistent averaging method, the free surface is smoother, see Fig. 4(b), and agrees much better with experimentally observed fluid distributions.

5. Validation for confined flow: sloshing experiment

The sloshing fluid motion in partially-filled LNG (liquefied natural gas) tanks is an example of two-phase flow with complex interaction between both phases. The fluid motion in these tanks is investigated because of impact loads on tank walls and its effect on ship motion. To study the sloshing behavior, both numerical simulations and model experiments have been carried out [53,54].

5.1. Setup of the model experiments

The model tests on scale 1:10 have been carried out primarily to generate validation material for the numerical method. To match simulation and experiment, the numerical simulations are carried out on the same scale as the model experiments. The model experiments use water for the liquid phase. The setup has been designed

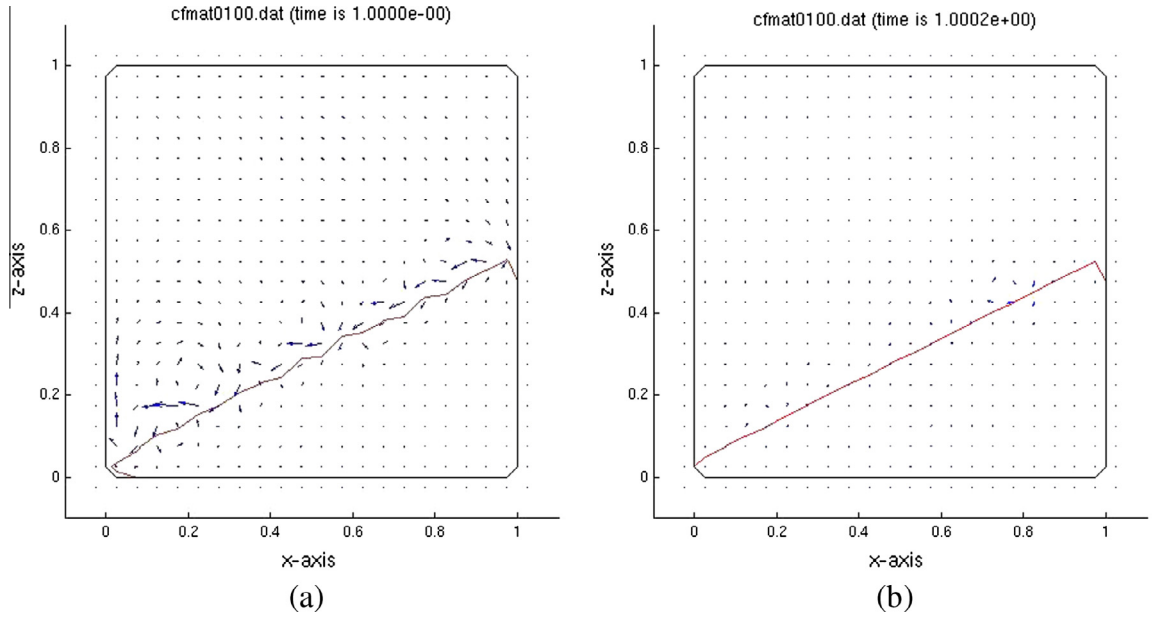

Fig. 3. Spurious velocities due to cell-weighted averaging of density (a) disappear when a gravity-consistent density averaging is used (b).

to resemble a 2D cross-section of a sloshing tank. Prior to the tests at DNV (Det Norske Veritas) in Oslo, the entire test setup (except the oscillator to move the tank) has been built and verified at the Maritime Research Institute Netherlands (MARIN). The sloshing tank model is based on an LNG tank inside a No. 96 LNG carrier; see Fig. 5. The tank is filled with water, while the front and back side are made of perspex to enable visualization of the fluid motion inside the tank.

Fig. 6 shows photographs of the sloshing experiments for a 10% filling ratio. As visible in these figures, the side walls of the tank are fitted with a number of measurement panels for piezo-resistive pressure transducers (4.5 mm diameter, 10 kHz), while the water height in the tank is measured by means of 12 resistance-type wave probes (100 Hz); some are indicated in Fig. 5right). The tests were visualized using a high-speed camera (100/200 Hz) and a digital color camera (25 Hz).

The global motion time traces of the tank, being measured during the experiments, are used as input for the simulations. The motion of the tank is considered as a moving coordinate frame in the simulations. The origin of the coordinate system is chosen at the center of the tank bottom. Displacement, velocity and acceleration of the moving coordinate frame have been derived from measured tank position time series. Careful differentiation of the position time series is required in order to acquire velocity and acceleration time series without artificial oscillations [51].

In the sequel of this paper we present results for a 10% filling ratio with regular as well as irregular tank motion. Experiments have also been conducted at higher filling ratios: 25%, 70% and 95%. Results hereof can be found in the PhD thesis [51].

5.2. Regular sway tank motion

Regular tank motion in combination with a low tank filling ratio of 10% leads to a fairly repetitive fluid distribution. The oscillation period is 11.0 s on full scale and about 3.0 s in the experiment, resulting in about 400 impacts on each side wall during the 20 min experiment. The fluid motion during the experiment is relatively calm with a bore after reversing the direction of tank motion and run-up against the tank walls. The ceiling of the tank is not touched by the liquid phase. We plan to make the experimental data for this test case available on the ComFLOW website [5]. The experimental data have been compared with numerical simulations on a grid of $195 \times 1 \times 135$ cells, i.e. a grid spacing of 2.0 cm. The effect of the grid spacing on the water height prediction will be described below.

Computation times vary considerably depending on the number of phases in the model and the applied spatial discretization scheme. For this case with low tank filling ratio, the number of active computational cells (and therewith the computation time) is much higher for two-phase flow simulations, whereas the flow field is resolved in only liquid cells for one-phase flow simulations. In addition, a second-order upwind spatial scheme is applied in combination with Adams–Bashforth time integration in the two-phase flow simulation, giving an upper limit of 0.25 on the CFL number [51]. Typical time steps are of the order of 10^{-3} s. On a 1 GB 2.8 GHz Pentium4 computer it takes about 10 h to simulate one minute of sloshing when the second-order upwind scheme is applied for two-phase flow.

Fig. 7 shows the water height development near the right tank wall (WH01). When examining photographs of typical fluid distributions in Fig. 6, it is expected that complex two-phase effects such as air entrapment do not play a significant role for this regular motion case. This expectation is confirmed by the water height development in Fig. 7(a), showing only small differences in wave run-up between the single-phase and two-phase simulations.

Although there is no air entrapment for the regular sway case, some interesting observations have been done when comparing various two-phase simulations. As described in Section 3.2, the second-order upwind scheme has been introduced in the numerical method to reduce artificial viscosity in the compressible air phase. Indeed, when examining Fig. 7(b), the run-up motion against the tank wall seems to be hindered by the numerical viscosity of the second phase when the first-order two-point upwind (B2) scheme is applied. Grid refinement will help to improve the agreement with experimental data [34], but Fig. 7(b) shows that it is more effective to use the second-order three-point upwind (B3) scheme.

Pressure signals from simulation and experiment are shown for two transducers in Fig. 8. Transducer P01 is located near the bottom of the tank wall and is always wet, while the more upwards

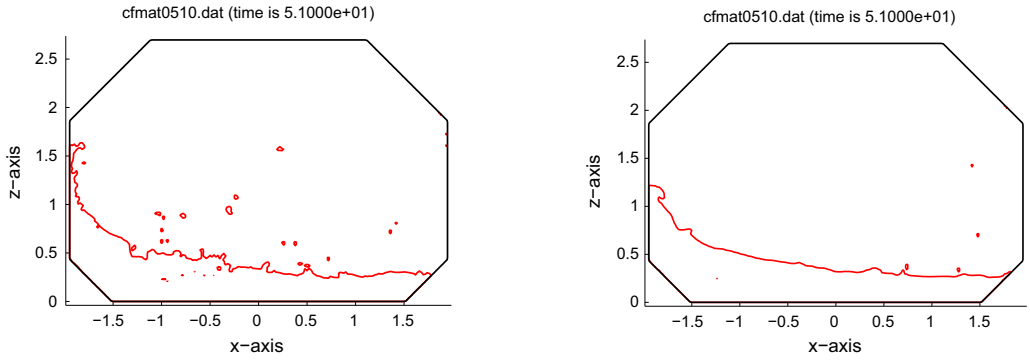

(a) Cell-weighted density averaging (b) Gravity-consistent density averaging

Fig. 4. Effect of the density averaging method on the free surface for a regular sway sloshing experiment with 10% filling ratio.

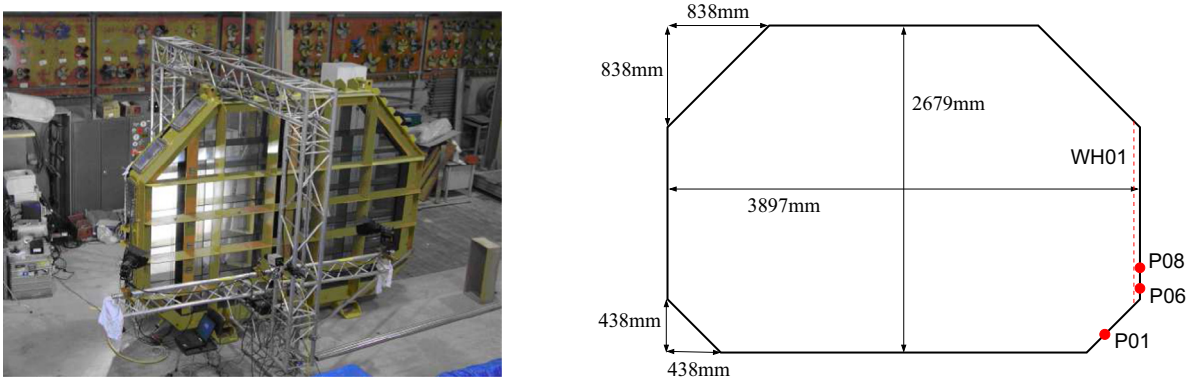

Fig. 5. Photograph of the setup for the sloshing model experiment (left). Dimensions of the tank and location of selected sensors (right).

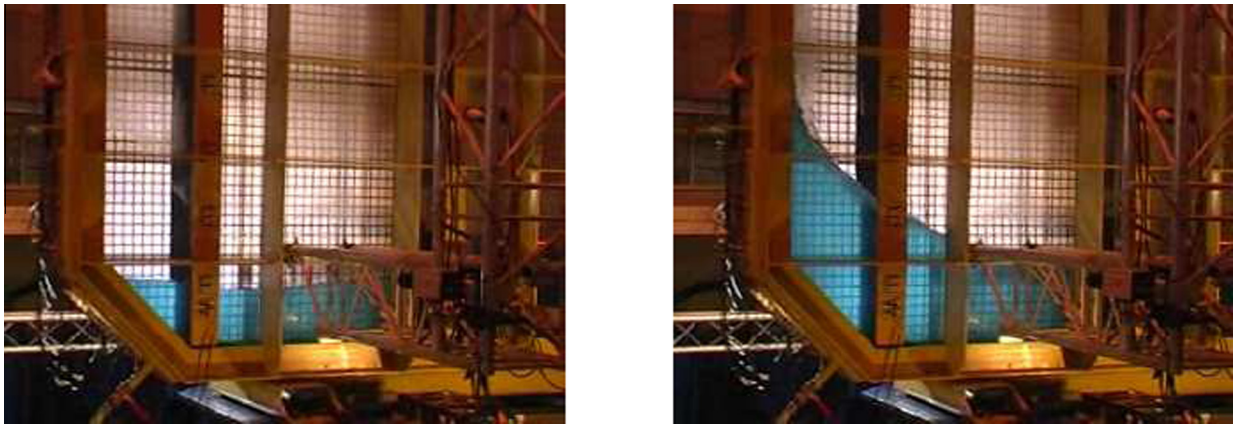

Fig. 6. Photographs of the 10% filling ratio sloshing model experiment. The left picture shows the fluid configuration at $t = 0$ s, the right picture the configuration at $t = 15$ s.

located transducer P06 is only wet during shorter periods (as expected when examining Fig. 7(a)). Both single- and two-phase flow simulations show a fair agreement with experimental data.

5.3. Irregular sway and roll tank motion

The second test case is an irregular sway and roll experiment with a filling ratio of 10%. The oscillation period is now 10.6 s on full scale, corresponding to 3.2 s on model scale. Compared with the regular sway experiment, the tank motion is less repetitive with wave breaking and air entrapment occurring occasionally. Two-phase phenomena such as air entrapment and entrainment are not observed during the first few sloshing periods, but occur later on in the experiment.

During the first sloshing periods, the level of run-up against the tank wall varies considerably, see Fig. 9(a). Simulation and experiment are in phase, but the one-phase simulation overestimates the run-up against the tank wall. This discrepancy might be related to the liquid motion that is not damped at all by the void in the remaining part of the computational flow domain. Also, the effect of aeration is not included in the computational model. The second phase is more viscous and heavier in the two-phase simulation, leading to a better agreement between numerically predicted and experimentally observed water heights.

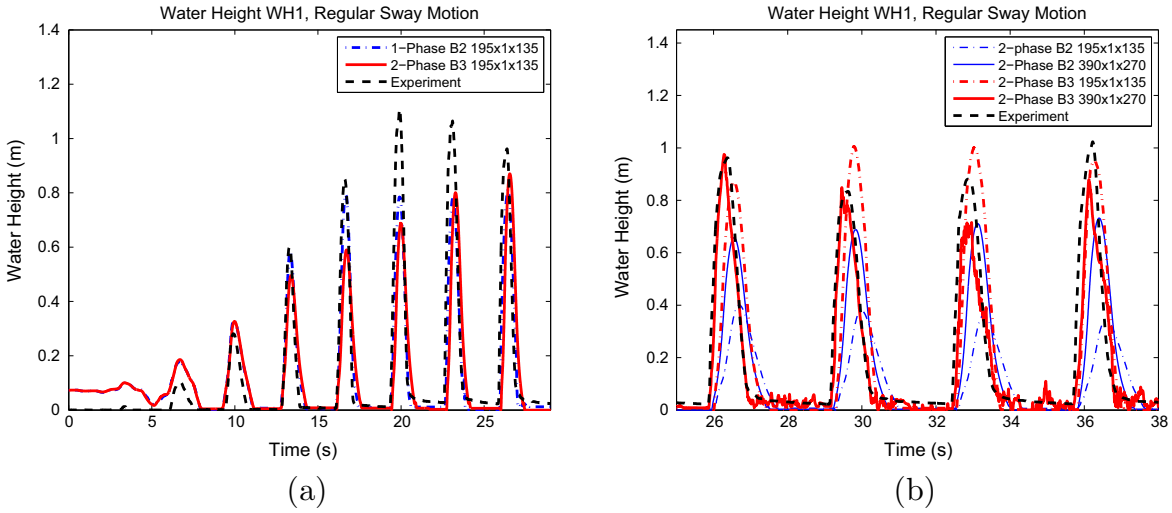

Fig. 7. Water height development for 10% filling ratio regular sway test at the tank wall WH01 ($x = 1.89$ m) during start-up and for various two-phase simulations right after initialization.

Fig. 9(b) shows the pressure development at transducer P01, located near the lower corner of the tank wall. When studying the pressure development at the tank wall, similar conclusions as for the water height development can be drawn. The over-estimated run-up motion in the one-phase simulation translates into peak pressures well above the experimentally observed values. Numerical pressure spikes are observed occasionally and are related to mass conservation problems in case of rapid transition from empty (void) cells to fluid cells. The pressure has to 'work' to achieve mass conservation for these cases, which manifests itself in spikes in the pressure signal. The two-phase simulation gives a better pressure prediction, although some short-during pressure spikes are also observed here.

After start-up of the sloshing motion during the first few periods of the experiment, the irregularity of the sloshing motion results in an alternation of periods with an almost flat horizontal free surface and periods with violent flow conditions. To study the effects of air entrapment and the capability of the numerical method to simulate these effects, one typical impact at $t = 140$ s is selected to be studied in more detail.

Fig. 10 shows some video frames of the experiment before, during and just after air entrapment. The entrapped air pocket with a diameter of $O(10^{-1})$ m is only present during a short period of $O(10^{-1})$ s, being compressed quickly by the water that is running up against the tank wall. The pressure development is considered for transducers P01, below the entrapped air pocket, and P08, just above the pocket.

For transducer P01, the one-phase simulation shows a number of pressure spikes that are present in neither the two-phase simulation nor the experiment, see Fig. 11. Furthermore, there is a (small) time lag between the one-phase simulation and the experiment, while the two-phase simulation shows a pressure peak simultaneously with the pressure peak in the experiment. The same observations regarding pressure development can also be done for pressure transducer P08. The water front reaches the transducer 'in time' for the two-phase simulation, while the one-phase simulation lags behind on the experiment. Also, the magnitude of the impact pressure peak is predicted better by the two-phase simulation.

6. Validation for open flow domain: wave run-up experiment

The effects of two-phase flow with respect to the propagation of waves in a domain with open boundaries are examined by investigating the wave run-up against a semi-submersible structure. Model experiments have been carried out at MARIN to provide

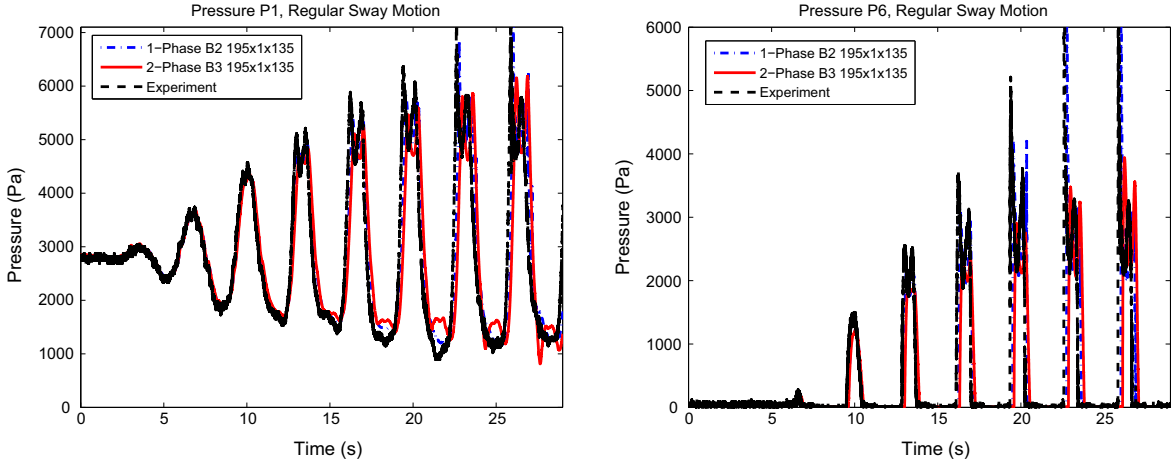

Fig. 8. Pressure development for regular sway 10% filling ratio tests at transducers P01 ($x = 1.656$ m, $z = 0.152$ m) and P06 ($x = 1.948$ m, $z = 0.531$ m).

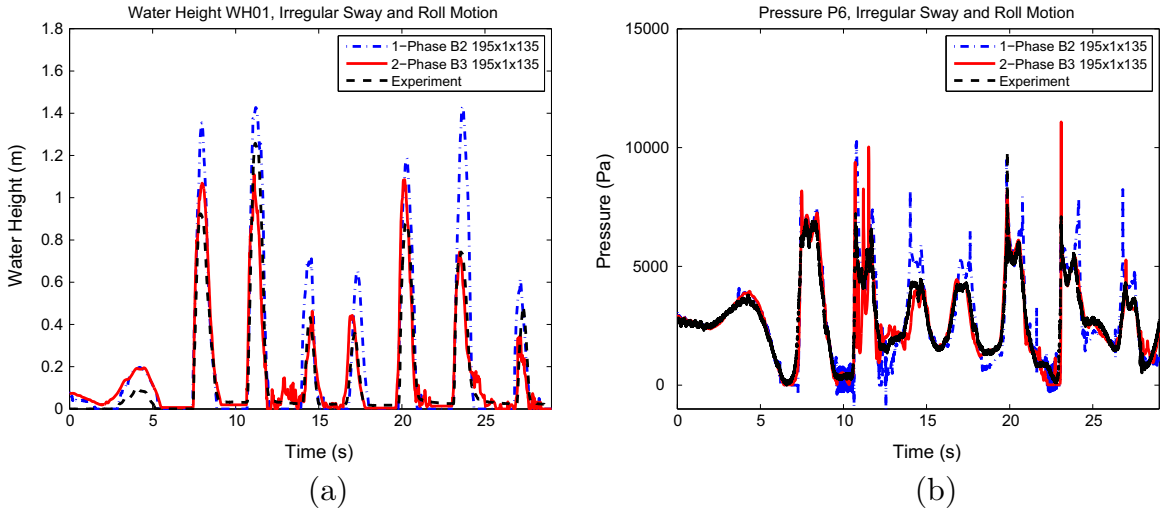

Fig. 9. Water height development for 10% filling ratio irregular sway and roll test at the tank wall WH01 ($x = 1.89$ m) and pressure signal at transducer P01 ($x = 1.656$ m, $z = 0.152$ m).

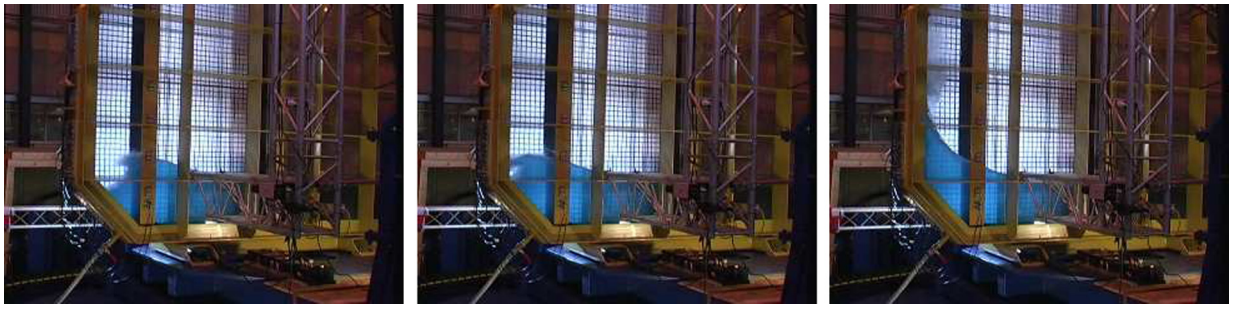

Fig. 10. Video frames of irregular 10% irregular sway and roll test at $t \approx 140$ s: just prior, during and after air entrapment at the tank wall.

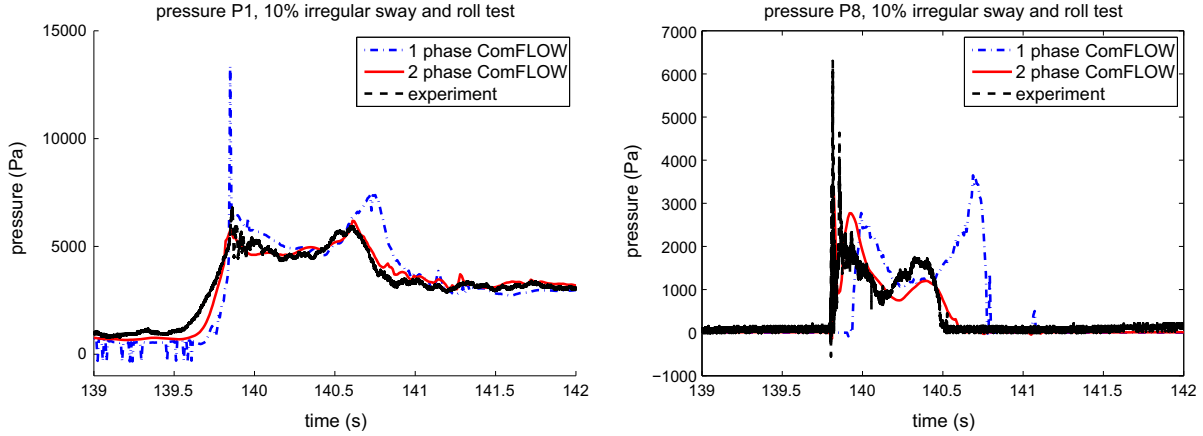

Fig. 11. Pressure development for transducers P01 ($x = 1.656$ m, $z = 0.152$ m) and P08 ($x = 1.948$ m, $z = 0.695$ m) during the air entrapment case shown in Fig. 10.

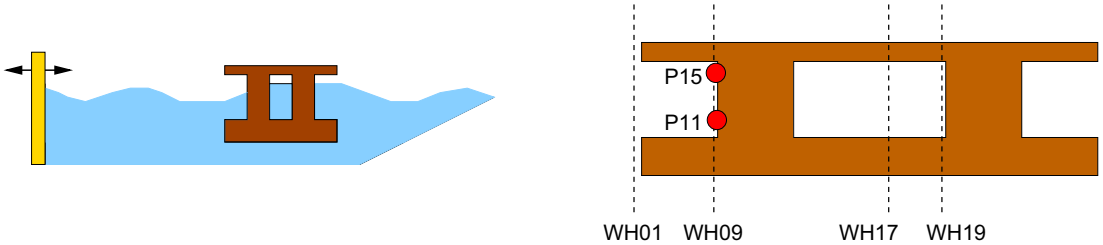

Fig. 12. Schematization of the wave run-up test setup (left) and position of selected wave probes and pressure transducers (right).

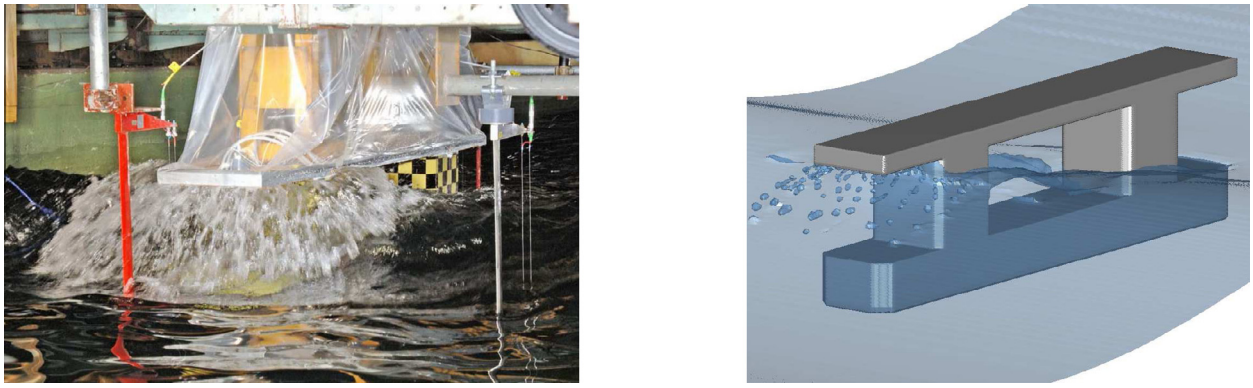

Fig. 13. Wave run-up against a semi-submersible: snapshots of experiment and simulation.

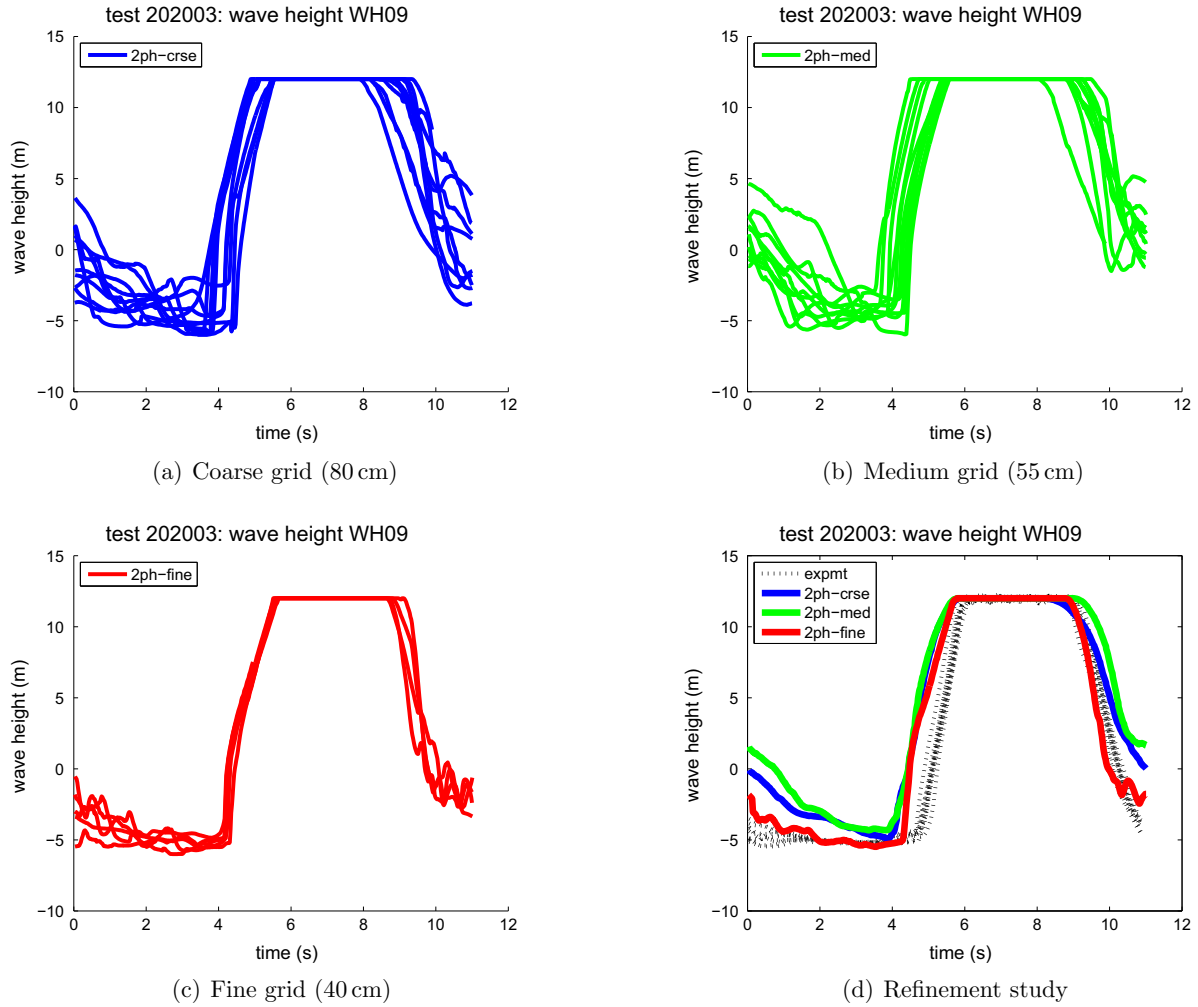

(a) Coarse grid (80 cm) (b) Medium grid (55 cm)

(c) Fine grid (40 cm) (d) Refinement study

Fig. 14. Variation of the numerical wave height at WH09 over the periods, plotted modulo the wave period, for the coarse (a), medium (b) and fine grid (c). The average results for the three grids versus experiment is shown in (d).

validation material for various aspects of the numerical method, such as the wave run-up effects and the impact loading on an offshore structure. For this flow case, an extensive assessment of numerical and experimental uncertainty is included below.

6.1. Positioning of the structure in the model basin

The setup of the wave run-up model experiment is sketched in Fig. 12. The experiment is carried out on a scale of 1:50. A semi-submersible with a typical (but simplified) geometry is located in the center of the flow domain. On full scale, it has a length of 114.5 m, a width of 17.5 m, a height of 28.0 m and a draft of 16.0 m. The semi-submersible consists of two columns, one pontoon and an (extended) deck box. The model is constructed as a rigid object made of wood (see Fig. 13).

The waves in the experiment are generated by a flap-type wave generator, creating waves by translational motion. The basin width is 4 m, which is equal to 200 m on full scale, with solid side walls.

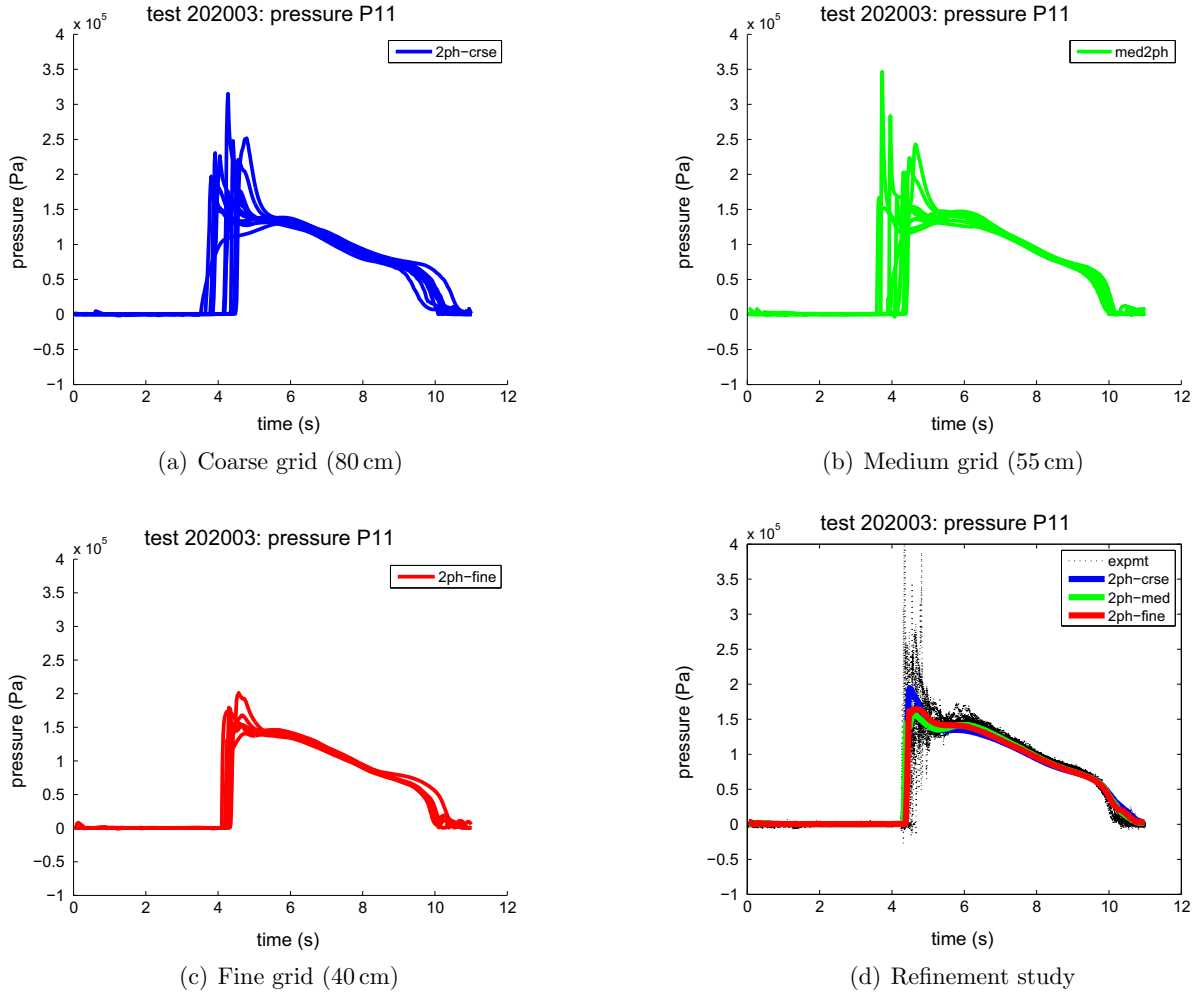

(a) Coarse grid (80 cm) (b) Medium grid (55 cm)

(c) Fine grid (40 cm) (d) Refinement study

Fig. 15. Variation of the numerical pressure at P11, plotted modulo the wave period, for the coarse (a), medium (b) and fine grid (c). The average results for the three grids versus experiment is shown in (d).

In the experiment, a beach is located downstream of the object to damp the motion of outgoing waves and to prevent wave reflections. The incoming wave has a full scale wave height of 14.7 m and a wave period of 11.0 s. To measure the wave elevation at several positions, an array of resistance type wave probes (100 Hz) is placed in the basin, most of them in front of and between the two columns. The pressure is monitored by 28 piezo-resistive transducers (5 kHz) that are fitted on the semi-submersible.

6.2. Wave run-up: grid refinement

In describing the wave motion in the simulation, the boundaries of the flow domain are brought closer to the structure than in the experiment to reduce computational costs. The computational domain is 400 m long, 200 m wide and vertically reaches 90 m into the water and 24 m into the air. Its inflow boundary is located at 240 m from the center of the semi-submersible (i.e. at 182.75 m from its front). To facilitate this decreased distance between the wave maker and the semi-submersible in the simulations, the incoming waves have been analyzed by wave calibration tests (without semi-submersible in the flow) to establish a representative incoming computational wave [23]. The generated incoming wave is modeled as a 5th-order Stokes wave, with wave parameters depending on the experiment. In particular, the period and the wave amplitude have been determined by comparing time traces of the wave height in a point 64.25 m in front of the semi-submersible. Note that the shape of the experimental wave differs from a theoretical Stokes wave, which is clearly visible in the wave height in probe WH01, just 9.90 m in front of the object. The wave crests correspond nicely, but there is a clear difference in the troughs. This has to be taken into account when comparing the simulations with the model tests.

The numerical simulations have been carried out on three different, stretched grids of increasing grid density: $180 \times 40 \times 60$, $270 \times 60 \times 90$ and $360 \times 80 \times 120$ grid cells in (horizontal) x-, (spanwise) y- and (vertical) z-direction. The grid sizes near the semi-submersible are about 80 cm, 55 cm and 40 cm, respectively, in all three directions. Two flow models have been used: an incompressible one-phase model and a compressible two-phase model, both with second-order upwind spatial discretization and Adams–Bashforth time integration. A numerical Sommerfeld condition is applied at the outflow boundary and the simulations are carried out for several wave periods (5–10 periods, depending upon the size of the computational grid).

Before interpreting the numerical results in physical terms, we first give an impression of the numerical error in the simulations. For WH09 and P11 (both at the first column) results are shown over a number of periods (again modulo the wave period) for all three grids in Figs. 14 and 15. Considerable scattering over the individual periods can be seen. We see in Figs. 14(a) and 15(d)) that the numerical sensitivity is comparable to the physical sensitivity of the flow, showing that there is no excessive numerical damping

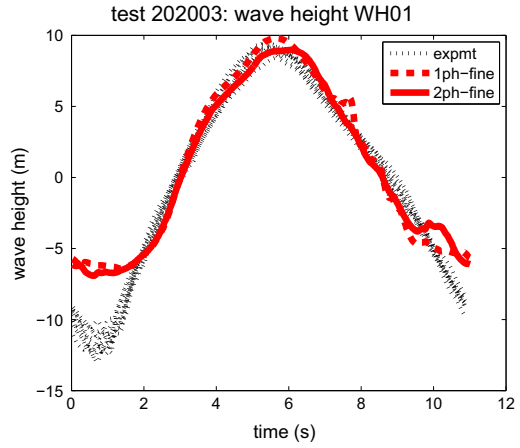

(a) Incoming wave.

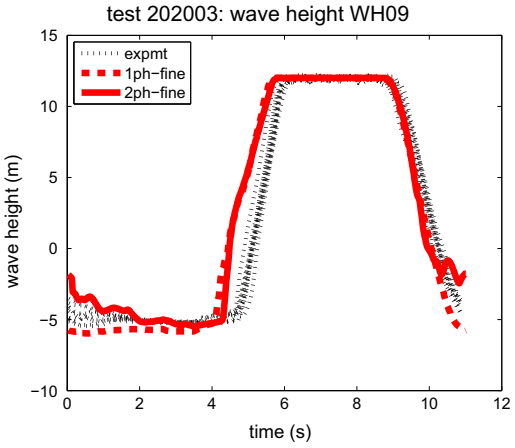

(b) Run-up at first column.

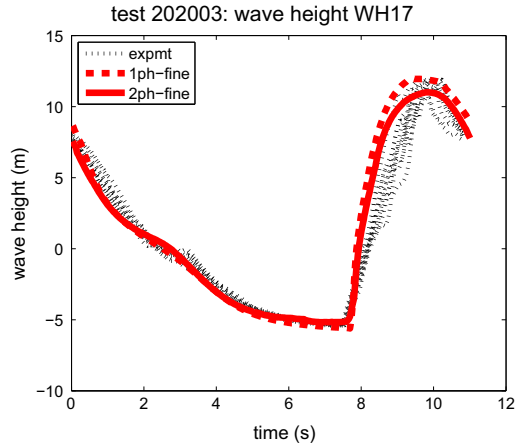

(c) Wave height between columns.

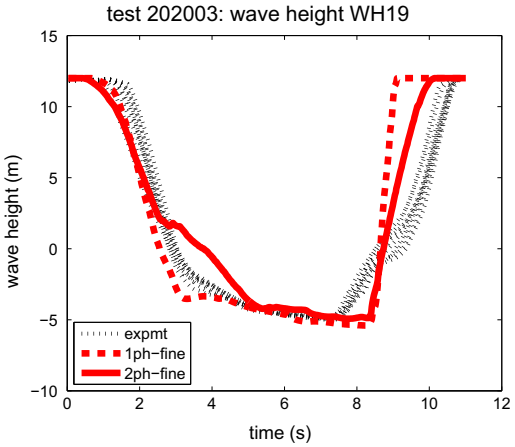

(d) Run-up at second column.

Fig. 16. The wave height development in one-phase and two-phase simulations compared with experimental data at four different locations (see Fig. 12(b)): (a) incoming wave: $x = -61.15$ m (WH01), (b) run-up at first column: $x = -39.76$ m (WH09), (c) wave height between columns: $x = 5.31$ m (WH17) and (d) run-up at second column: $x = 21.24$ m (WH19).

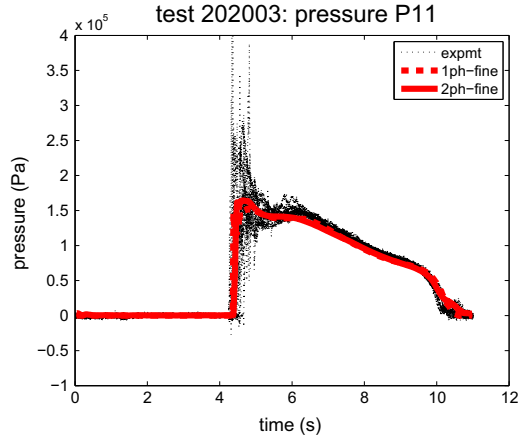

(a) Bottom of first column.

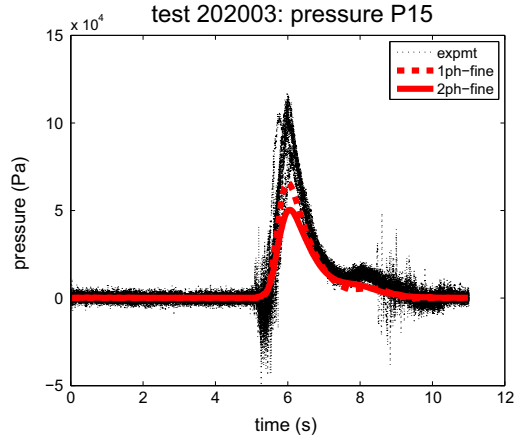

(b) Top of first column.

Fig. 17. The pressure development in one-phase and two-phase simulations compared with experimental data at two different locations (see Fig. 12(b)) along the front of the first column: (a) near the bottom of the column (P11); (b) near the top (P15).

mechanism (like an overdose of artificial numerical diffusion) present. On the finer grids, where the violent free-surface motion is better resolved, the scattering over the periods becomes smaller. The spreading of the computational results is typical of VOF-based flow simulations, where small deviations can lead to 'discontinuous' changes in cell labels, after which a complete cell is treated differently.

For the comparison with the experimental data, averages over the simulated time periods have been used. For the three consecutive grids, this comparison is shown in Figs. 14(a) and 15(d), respectively. In these graphs, 10 periods of the experiment (between 944 s and 1054 s) have been plotted, to indicate the scatter in the experimental results.

With respect to the wave height in WH09, the fine grid simulation (40 cm grid size) is clearly the best: a smaller grid size is better capable of resolving the thin water layers during run-up (which does not come as a surprise). The pressure results in P11 for the various grids agree closer with each other: their mutual differences are smaller than the scatter in the experimental results. Thus, the necessity of sufficiently-resolved simulations seems less important for predicting the pressure. Recall that the incoming 5th-order Stokes wave in the simulations is not exactly equal to the incoming wave in the experiments. Thus differences between simulation and experiment are to be expected (which does not make the validation easier...).

6.3. Wave run-up: discussion of results

After having obtained an indication of the 'numerical noise' in the simulations, the fine-grid results of the one- and two-phase flow simulations are compared with experiment in more measuring points. These results will be discussed in more physical terms.

During wave impact, the first column is completely covered by liquid, while also the bottom of the extended deck is hit by the impacting wave. Fig. 16 shows the wave height development for the incoming wave (WH01), at the first column (WH09), between the columns (WH17) and at the second column (WH19). The results on the fine grid from a one-phase simulation and a two-phase simulation are shown in comparison with the experimental data.

The overall agreement between the wave heights in the simulations and the experiment is quite good. The wave heights in Fig. 16 show a periodic variation between zero and maximum filling ratios at the columns of the semi-submersible (ranging from $z = -6$ m to $z = 12$ m). For the incoming wave (WH01), there is a clear difference between the wave troughs of simulations and experiment. This has to do with the incoming 5th-order Stokes wave being calibrated on basis of the wave crests. When the flow develops further downstream along the structure, this difference decreases, as can be seen from the wave height just in front of the first column (WH09).

Between the two columns (WH17) of the semi-submersible, the wave height in both simulations is quite close to the experimental values. Near the second column (WH19), the two-phase wave peaks agree better (compared to the one-phase simulation) with the experiment, while the agreement is worse for the two-phase wave troughs. Overall, the one-phase and two-phase flow results are quite comparable. This is to be expected, as there are no dominant regions of entrapped air, as was the case in the sloshing example from the previous section.

The pressure development near the bottom (P11) and the top (P15) of the first column of the semi-submersible is shown in Fig. 17. For transducer P11, the short-lasting pressure peaks of the experiment are also visible in the simulations. Near the top of the first column, at transducer P15, there are more pronounced differences between the one- and two-phase simulations and the experiment. The peak pressure values in the simulations are relatively low, which can be attributed to the limited number of grid cells along the column. Grid refinement around the column can improve predictions of the wave run-up height and the pressure [34]: we will report on more detailed simulations in [35]. The difference in peak pressure values between one- and two-phase simulations can possibly be attributed to the cushioning effect of the air between the wave front and the deck of the semi-submersible, reducing the flow velocity and hence the peak pressure level at impact. For one-phase flow, the water is not decelerated by the compressible air, leading to a slightly earlier and higher impact on the pressure transducers.

7. Concluding remarks

Various offshore test cases have been simulated with the CFD method ComFLOW. In case of complex hydrodynamic phenomena, such as wave breaking and air entrapment, it is beneficial to carry out two-phase flow simulations. The dynamics of the compressible second phase affects the fluid distribution and the pressure level of the liquid phase. Due to the presence of the second phase, the fluid density varies up to a factor of 1000 across the free surface, imposing a challenge to stability and convergence of the numerical method. Rewriting the pressure Poisson equation, application of an appropriate pressure solver and the use of a gravity-consistent density averaging method are essential ingredients of the numerical method to be able to handle these large density variations.

For confined flows, e.g. sloshing fluid in LNG tanks, highly unsteady flow phenomena such as air entrapment are resolved by the two-phase flow modeling in the numerical method. Only for regular sway motion in combination with a low tank filling ratio it is sufficient (and quicker in terms of computational time) to model the dynamics of the liquid phase only. When simulating the flow in open domains, additional difficulties show up, such as wave definition and inflow and outflow boundary conditions. Wave damping and reflection should be treated carefully for these cases. For the simulation of wave run-up against a semi-submersible offshore structure there is a good prediction of the flow around the structure, although a fine grid is needed to predict the impact on the columns and the deck of the structure accurately.

Acknowledgements

This research has been supported by the Dutch Technology Foundation STW, applied science division of NWO and the technology programme of the Ministry of Economic Affairs in The Netherlands (GWI.6433).

References

[1] Afkhami S, Bussmann M. Height functions for applying contact angles to 2D VOF simulations. Int J Numer Meth Fluids 2008;57(4):453–72.
[2] Botta EFF, Ellenbroek MHM. A modified SOR method for the Poisson equation in unsteady free-surface flow calculations. J Comput Phys 1985;60:119–34.
[3] Brodtkorb B. Prediction of wave-in-deck forces on fixed jacket-type structures based on CFD calculations. In: 27th int conf offshore mechanics and arctic eng, OMAE2008. Estoril (Portugal); June 15–20, 2008 [paper OMAE2008-57346].
[4] Buchner B. Green water on ship-type offshore structures. PhD Thesis. University of Delft; November 2002.
[5] ComFLOWwebsite. <www.math.rug.nl/~veldman/comflow/comflow.html>.
[6] Danmeier DG, Seah RKM, Finnigan T, Roddler D, Abault A, Vache M, et al. Validation of wave run-up calculation methods for a gravity based structure. In: 27th int conf offshore mechanics and arctic eng. OMAE2008. Estoril (Portugal); June 15–20, 2008 [paper OMAE2008-57625].
[7] Deane GB, Stokes MD. Scale dependence of bubble creation mechanisms in breaking waves. Nature 2002;418:839–44.
[8] Dröge M, Verstappen R. A new symmetry-preserving Cartesian-grid method for computing flow past arbitrarily shaped objects. Int J Numer Meth Fluids 2005;47:979–85.
[9] Düz B, Huijsmans RHM, Veldman AEP, Borsboom MJA, Wellens PR. An absorbing boundary condition for regular and irregular wave simulations. In: Eça L et al., editors. MARINE 2011, IV international conference on

computational methods in marine engineering, selected papers. Computational methods in applied sciences, vol. 29. Berlin: Springer; 2001. p. 31–46.
[10] Düz B, Huijsmans RHM, Borsboom MJA, Wellens PR, Veldman AEP, Luppes R. Generating and absorbing boundary conditions for free-surface flow simulations in offshore applications. In: 34th conf ocean, offshore and arctic eng. OMAE2015. St John's (Canada); May 31–June 5, 2015 [paper OMAE2015-41577].
[11] Faltinsen OM. Sea loads on ships and offshore structures. Cambridge University Press; 1999.
[12] Fontaine E, Landrini M, Tulin MP. On modeling the post breaking phase: splashing. In: Miloh T, Zilman G, editors. Proc 15th int workshop water waves and floating bodies. Caesarea; February 27–March 1, 2000.
[13] Forristal G. Wave crest height and deck damage in hurricanes Ivan, Katrina and Rita. In: Proc OTC. Houston (Houston); 2007.
[14] Francois MM, Cummins SJ, Dendy ED, Kothe DB, Sicilian JM, Williams MW. A balanced-force algorithm for continuous and sharp interfacial surface tension models within a volume tracking framework. J Comput Phys 2006;213:141–73.
[15] Gerrits J, Veldman AEP. Dynamics of liquid-filled spacecraft. J Eng Math 2003;45:21–38.
[16] Greco M, Faltinsen OM, Landrini M. Numerical simulation of heavy water shipping. In: Proc 17th workshop water waves and floating bodies. Cambridge (UK); 14–16 April 2002.
[17] Harvie DJE, Davidson MR, Rudman M. An analysis of parasitic current generation in Volume of Fluid simulations. Appl Math Model 2006;30:1056–66.
[18] Haver S. Evidences of the existence of freak waves. In: Ifremer, editor. Rogue waves 2000, Proc of int workshop. Brest (France); 29–30 November, 2000. p. 129–40.
[19] Hirt CW, Nichols BD. Volume of Fluid (VOF) method for the dynamics of free boundaries. J Comput Phys 1981;39:201–25.
[20] van't Hof Bas, Veldman Arthur EP. Mass, momentum and energy conserving (MaMEC) discretizations on general grids for the compressible Euler and shallow water equations. J Comput Phys 2012;231:4723–44.
[21] Iglesias AS, Rojas LP, Rodriguez RZ. Simulation of anti-roll tanks and sloshing type problems with smoothed particle hydrodynamics. Ocean Eng 2004;31:1169–92.
[22] Iwanowski Bogdan, Lefranc Marc, Wemmenhove Rik. CFD simulation of wave run-up on a semi-submersible and comparison with experiment. In: 28th conf on ocean, offshore and arctic eng, OMAE2009. Honolulu (USA); May 31–June 5, 2009 [paper OMAE2009-79052].
[23] Iwanowski Bogdan, Lefranc Marc, Wemmenhove Rik. Numerical simulation of sloshing in a tank, CFD calculations against model tests. In: 28th conf on ocean, offshore and arctic eng, OMAE2009. Honolulu (USA); May 31–June 5, 2009 [paper OMAE2009-79051].
[24] Khayyer A, Gotoh H. Modified Moving Particle Semi-implicit methods for the prediction of 2D wave impact pressure. Coast Eng 2009;56(4):419–40.
[25] Kleefsman KMT. Water impact loading on offshore structures – a numerical study. PhD thesis. University of Groningen; 2005.
[26] Kleefsman KMT, Fekken G, Veldman AEP, Buchner B, Iwanowski B. A volume-of-fluid based simulation method for wave impact problems. J Comput Phys 2005;206:363–93.
[27] Lande O, Johannessen TB. CFD analysis of deck impact in irregular waves. In: 30th conf on ocean, offshore and arctic eng, OMAE2011. Rotterdam (Netherlands); June 19–24, 2011 [paper OMAE2011-49418].
[28] Loots GE, Hillen B, Veldman AEP. The role of hemodynamics in the development of the outflow tract of the heart. J Eng Math 2003;45:91–104.
[29] Maurits NM, Loots GE, Veldman AEP. The influence of vessel wall elasticity and peripheral resistance on the flow wave form: CFD model compared to in-vivo ultrasound measurements. J Biomech 2007;40(2):427–36.
[30] van Mourik S, Veldman AEP, Dreyer M. Simulation of capillary flow with a dynamic contact angle. Microgravity Sci Technol 2005;17(3):91–8.
[31] Monaghan JJ. Simulating free surface flows with SPH. J Comput Phys 1994;110:399–406.
[32] Nouri C, Luppes R, Veldman AEP, Tuszynski JA, Gordon R. Rayleigh instability of the inverted one-cell amphibian embryo. Phys Biol 2008;5(1). article 010506.
[33] Peregrine DH. Water-wave impact on walls. Ann Rev Fluid Mech 2003;35:23–43.
[34] van der Plas P, van der Heiden HJL, Veldman AEP, Luppes R, Verstappen RWCP. Efficiently modeling viscous flow effects by means of regularization turbulence modeling and local grid refinement. In: Proc 7th int conf comp fluid dyn ICCFD7. Hawaii (USA); July 9–13, 2012 [paper ICCFD7-2503].
[35] van der Plas P, Veldman AEP, van der Heiden HJL, Luppes R. Adaptive grid refinement for free-surface flow simulations in offshore applications. In: 34th conf ocean, offshore and arctic eng, OMAE2015. St John's (Canada); May 31–June 5, 2015 [paper OMAE2015-42029].
[36] Rider WJ, Kothe DB. Reconstructing volume tracking. J Comput Phys 1998;141:112–52.
[37] Rozema W, Kok JC, Verstappen RWCP, Veldman AEP. A symmetry-preserving discretization and regularization model for compressible flow with application to turbulent channel flow. J Turbulence 2014;15:386–410.
[38] Rudman A. A volume-tracking method for incompressible multifluid flows with large density variations. Int J Numer Meth Fluids 1998;28:357–78.
[39] Shirani E, Ashgriz N, Mostaghimi J. Interface pressure calculation based on conservation of momentum for front capturing methods. J Comput Phys 2005;203:154–75.
[40] Skjelbreia L, Hendrickson JA. Fifth order gravity wave theory. In: Proc 7th coastal engineering conf. The Hague (Netherlands); 1960. p. 184–96.
[41] Trygvasson G, Bunner B, Esmaeeli A, Juric D, Al-Rawahi N, Tauber N, et al. A front-tracking method for the computations of multiphase flow. J Comput Phys 2001;169:708–59.
[42] Tsai W, Yue DKP. Computation of nonlinear free-surface flows. Ann Rev Fluid Mech 1996;28:249–78.
[43] Veldman AEP, Gerrits J, Luppes R, Helder JA, Vreeburg JPB. The numerical simulation of liquid sloshing on board spacecraft. J Comput Phys 2007;224:82–99.
[44] Veldman AEP, Lam K-W. Symmetry-preserving upwind discretization of convection on non-uniform grids. Appl Numer Math 2008;58:1881–91.
[45] Veldman AEP, Luppes R, Bunnik T, Huijsmans RHM, Düz B, Iwanowski B, et al. Extreme wave impact on offshore platforms and coastal constructions. In: 30th conf ocean, offshore and arctic eng, OMAE2011. Rotterdam (Netherlands); June 19–24, 2011 [paper OMAE2011-49488].
[46] Veldman AEP, Luppes R, van der Heiden HJL, van der Plas P, Düz B, Huijsmans RHM. Turbulence modelling, local grid refinement and absorbing boundary conditions for free-surface flow simulations in offshore applications. In: 33th conf ocean, offshore and arctic eng, OMAE2014. San Francisco (USA); June 8–13, 2014 [paper OMAE2014-24427].
[47] Veldman AEP, Vogels MES. Axisymmetric liquid sloshing under low gravity conditions. Acta Astronaut 1984;11:641–9.
[48] Verstappen RWCP, Veldman AEP. Data-parallel solution of the incompressible Navier–Stokes equations. In: Wesseling P, editor. High performance computing in fluid dynamics. Kluwer Academic Publishers; 1996. p. 237–60.
[49] Verstappen RWCP, Veldman AEP. Symmetry-preserving discretization of turbulent flow. J Comput Phys 2003;187:343–68.
[50] Wellens PR. Wave simulation in truncated domains for offshore applications. PhD thesis. Delft University of Technology; 2012.
[51] Wemmenhove R. Numerical simulation of two-phase flow in offshore environments. PhD thesis. University of Groningen; 2008.
[52] Wemmenhove R, Loots GE, Luppes R, Veldman AEP. Modelling two-phase flow with offshore applications. In: 24th int conf offshore mech arctic eng, OMAE2005. Halkidiki (Greece); 2005 [paper OMAE2005-67460].
[53] Wemmenhove R, Luppes R, Veldman AEP. Application of a VOF method to model compressible two-phase flow in sloshing tanks. In: 27th int conf offshore mech arctic eng, OMAE2008. Estoril (Portugal); 2008 [paper OMAE2008-57254].
[54] Wemmenhove R, Luppes R, Veldman AEP, Bunnik T. Numerical simulation and model experiments of sloshing in LNG tanks. In: Computational methods in marine engineering II. Barcelona (Spain); 2007.
[55] Wesseling P. Principles of computational fluid dynamics. Springer series in computational mathematics, vol. 29. Berlin: Springer; 2001.
[56] Youngs DL. An interface tracking method for a 3d Eulerian hydrodynamics code. Tech rep AWRE/44/92/35. Atomic Weapons Research Establishment (UK); 1987.